Cislunar Orbit Determination using passive RF sensors

François Thevenot
Safran Data Systems, Colombelles, France
Baptiste Guillot, Sebastien Herbiniere
Safran Data Systems, Colombelles, France

ABSTRACT

Cislunar activities are rapidly increasing because of multi-national interest to explore the lunar surface and beyond. Indeed, 2024 opened with the launch of Peregrine mission and SLIM's lunar landing in January, followed by Intuitive Machine's Nova-C lunar landing in February, the Chang'e 6 lunar landing in May with several missions still to come (Trailbrazer, VIPER, Blue Ghost, PRIME-1, …). As the frequency of cislunar missions increase the capability to accurately track them will be essential to safe and sustainable space operations. As space situational awareness continues to evolve and extends beyond Earth's orbit, Passive Radio Frequency (RF) technology is well suited to support this endeavor.
Passive RF technology offers many advantages:

- persistent tracking through weather and daylight exclusion times with a high revisit rate
- tracking of multiple frequency bands (S, X, C, Ku, Ka); enhancing its robustness
- technology is less prone to produce measurement's cross tags due to the signal footprint used to perform the measurements
- cross-correlation results in the production of two observables (TDOA and FDOA), each measurement giving access to different orbital parameters observability, increasing efficiency of the orbit determination process.

In this paper, we assess the global performance of Passive RF tracking for cislunar cases. We want to focus on the impact of the use of a long baseline configuration on the orbit determination performance. To do so, we will analyze the cislunar orbit determination performance on the Lunar Reconnaissance Orbiter (LRO) mission in two configurations: short baseline only and then a combination of short and long baseline. We will also present results obtained using real data from the Orion Artemis I mission.

1. INTRODUCTION

1.1 WeTrack presentation - Passive RF sensor

WeTrack is the Safran Data Systems (SDS) Passive Radio Frequency (RF) sensor implementation. It is a commercial data service for geosynchronous spacecraft tracking running for about 10 years.
Passive RF sensors rely on Time Difference Of Arrival (TDOA) and Frequency Difference Of Arrival (FDOA) measurement to achieve accurate spacecraft orbit determination. The Cross Ambiguity Function (CAF) of two different RF signals collected on two distant Earth stations (separated by about 300km) is used to measure TDOA and FDOA values. A minimum sensor architecture is made of three ground stations. Fig. 1 shows the system reduced to a single baseline of two ground stations.
High accuracy time and frequency sensor synchronization is achieved using GNSS constellations (GPS & GALILEO). All the stations of a cluster are pointing synchronously toward the same target to perform the acquisition of the signal of interest. Acquired signal snapshots are transferred to the computing center that computes the CAF estimation to determine the target's TDOA & FDOA (See Fig. 2).

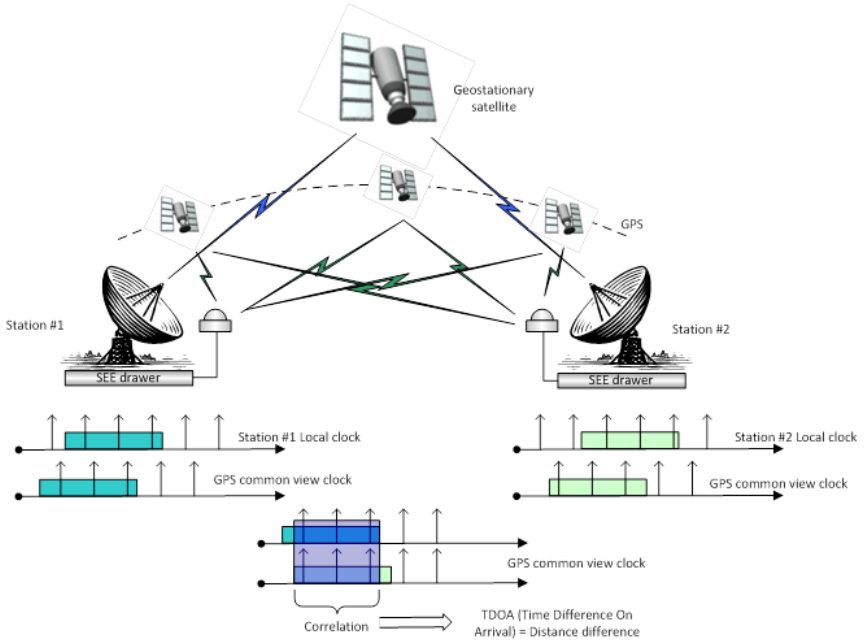

Fig. 1: WeTrack signal flow diagram

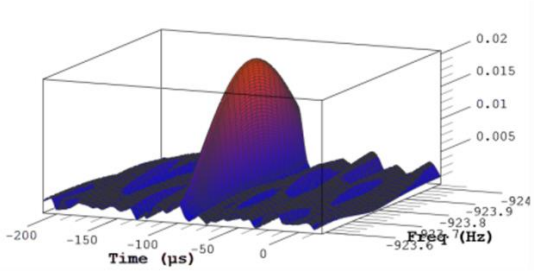

Fig. 2: Cross Ambiguity Function

Passive RF allows for:

- Diurnal (and night) measurements collection
- Fast cadence of collections (e.g., normal ops about every 40 minutes, intense collection every 5 minutes)
- Weather condition independent measurements collection
- Maneuver characterization
- Spacecraft RF behavior characterization
- Individual spacecraft identification

Safran Data Systems is currently integrating the LEO tracking capability to the WeTrack sensor network, leveraging the ability to perform some xGEO studies and experimentation. Table 1 lists the key ground station specifications.

Specification	**Value**
Azimuth travel	0° to 360°
Elevation travel	0° to 90°
Motion speed	36° deg/s
Acceleration	36° deg/s
Pointing accuracy	0.08deg
Frequency bands	S, C, X, Ku, Ka

Table 1: Passive RF receiving station specifications

The WeTrack worldwide sensor network enables small/medium (300 km) baseline passive RF measurement but also long baseline measurement reaching up to 12,500 km distance. Fig. 3 shows the global network map.

Fig. 3: WeTrack sensor network map

2. MOON CENTERED PROPAGATOR

For its space surveillance activities, Safran Data Systems developed its own orbital dynamics library. In the beginning WeTrack was designed to track Earth orbiting objects and so an Earth-centric framework was appropriate. With the growing interest in cislunar activities, this library has been enhanced to allow the computation of non-earth orbiting object trajectories and particularly for moon-centered ones. Validation of such a propagator is key and needs to be performed very cautiously.

2.1 Moon-centered propagator implementation

2.1.1 Definition of Moon Frames

Two intuitive frames are introduced:

- Inertial moon centered frame: this corresponds to a GCRF[1] with its origin at the Moon.
- Body fixed frame: this frame is attached to the Moon, with True equator and axes corresponding to Moon Principal Axes. This corresponds to what we can call a 'Moon True of Date' (MTOD).

The conversion between these two frames involves the so-called Moon libration angles (See Fig. 4).

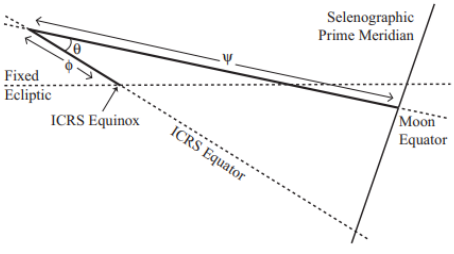

Fig. 4: ICRF[2] to Moon Principal Axes transformation

[1] GCRF: Geocentric Celestial Reference Frame
[2] ICRF: International Celestial Reference Frame

These angles are of paramount importance for any accurate implementation of a Moon propagator and one has imperatively to use its accurate computation. Indeed, there exists two classical ways of computing the Moon libration angles:

- Using the JPL DE ephemerides
- Using the IAU working group on cartographic coordinates and rotational elements of the planets and satellites (WGCCRE) analytical recommendation

As mentioned by the IAU working group itself, the latter angles are accurate up to 0.1° [1]. Such a difference corresponds to an error of 3km at the Moon's surface and should only be used for mission analyses purposes and not for any orbit determination purpose. It is therefore of uttermost importance when using a moon propagator to ensure that the right computation of the Moon libration angles is used.

2.2 Moon-centered propagator validation

To validate Safran Data Systems moon-centered propagator, we performed a fit of a reference ephemeris based on position and velocity measurements coming from this reference ephemeris. We compared our solution to the reference ephemeris and the solution given by Orekit, a widely used orbital dynamics library.
The fit parameters are the following:

- Reference ephemeris: Lunar Reconnaissance Orbiter's (LRO) JPL Horizons
- Fit period: 15/07/2009 – 16/07/2009
- Measurements used: position and velocity
- Estimated parameters : initial position and velocity, solar radiation pressure coefficient
- Lunar potential : GRAIL350A, order 150 and degree 150, with permanent tide

We can see in Fig. 5 that the SDS Moon propagator fits the JPL ephemeris with a RMS error of roughly 8m over the fit period, which fully validates the model used and the Moon libration implementation.
On the Orekit side, we notice that the RMS error in position is of 83m over the fit period which is quite good. But we notice clearly that the error lies in the orbital plane orientation (the error in inclination and right ascension of ascending node), suggesting a wrong implementation in the Moon libration angles.

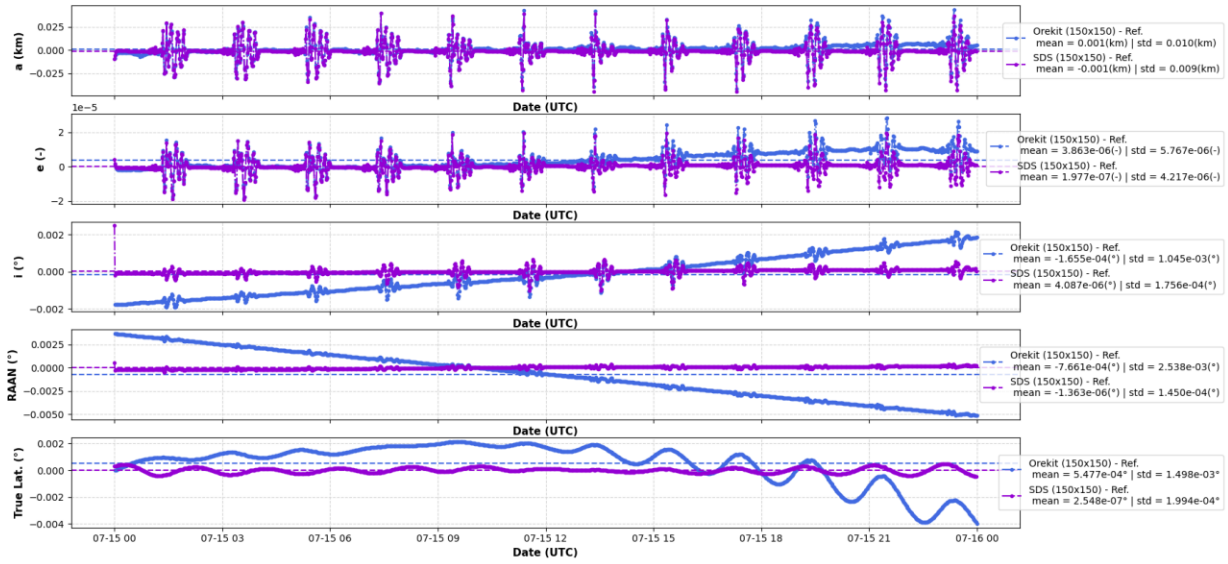

Fig. 5: Comparison of SDS and Orekit fitted ephemerides with respect to a reference ephemeride

Indeed, comparing the Orekit libration angles and SDS ones (using JPL ephemerides), with an external reference (ESA WebGeocalc tools), we can clearly see (See Fig. 6 and Fig. 7) that SDS and ESA WebGeocalc tools agrees perfectly (~5e-5°), compared to Orekit which bears a difference of about 0.08° with respect to the reference, consistent with IAU WGCCRE model accuracy.

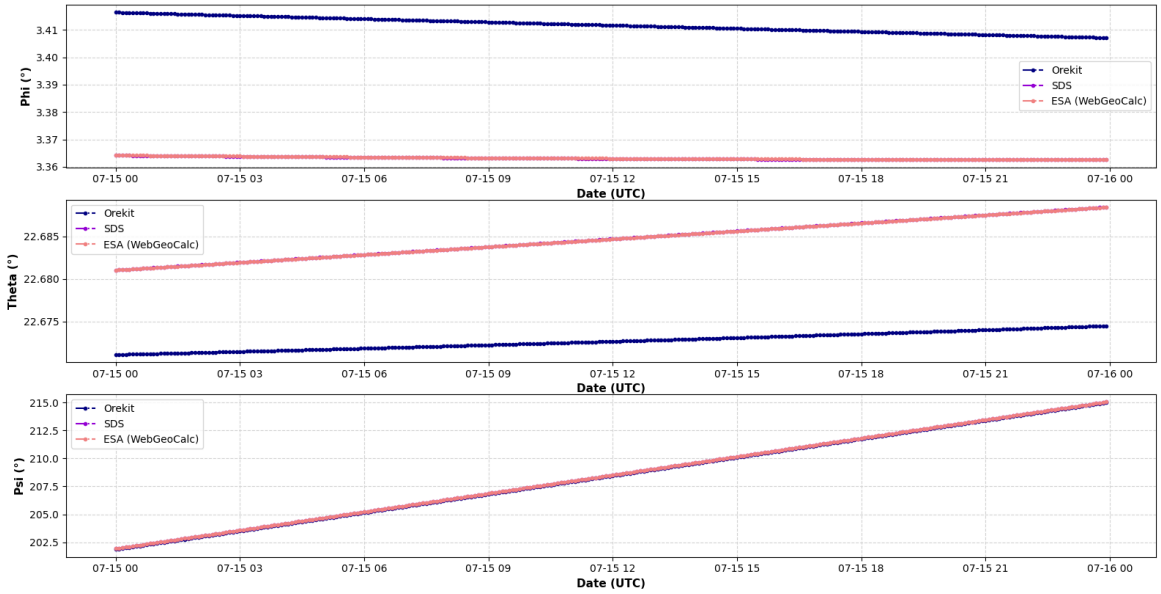

Fig. 6: Moon libration Euler angles (SDS, Orekit and reference)

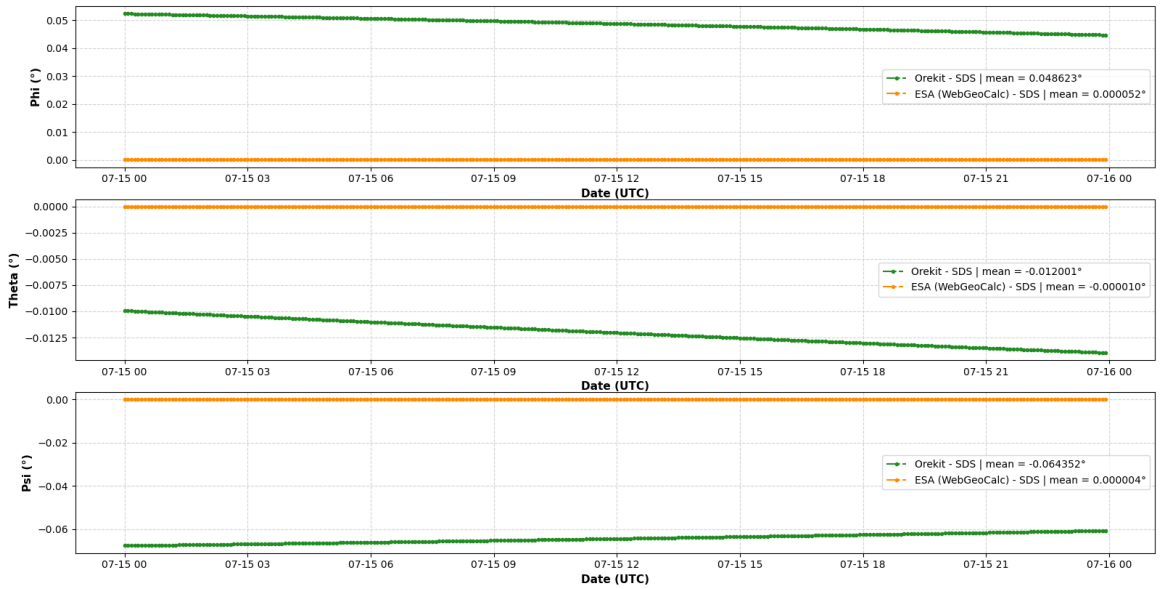

Fig. 7: Comparison of moon libration angles with reference

In conclusion, one has to be careful when implementing the Moon libration angles for orbit determination purposes around the Moon.

3. CISLUNAR PASSIVE RF ORBIT DETERMINATION

3.1 Orbit determination parameters

In the following section, all the orbit determinations are performed based on simulated measurements on the JPL Horizons reference trajectory.
The measurements considered are TDOA and FDOA, generated on Safran Data System's ground stations' network described in Table 2.
This network consists of ground stations distributed in clusters over four regions (CONUS, EMEA, APAC, Oceania-Pacific).
The measurements are perturbed with Gaussian noise and some outliers are randomly generated to make measurements as realistic as possible. An uncertainty is also set on the TDOA bias (FDOA has no intrinsic bias) to account for synchronization error and atmospheric uncertainties (tropospheric and ionospheric effects). All these data are summarized in Table 3.

Subnet	Number of ground stations
CONUS	4
EMEA	4
APAC	4
Oceania Pacific	3

Table 2: Number of ground stations by region

Data		Standard deviation	
		Short baseline configuration	Long baseline configuration
TDOA (ns)		5	5
FDOA (Hz)		0.168 (X-band)	0.168 (X-band)
TDOA bias (ns)	synchronization uncertainty	5	10
	atmospheric effect	1.5	1.5
	Total (RSS[3])	5.22	10.11

Table 3: Measurement noise parameters

The period of the analyses covers the period from 20th September 2009 to 15th February 2010. This period was chosen because it corresponds to a period in which there is public information on the LRO station-keeping [2] and then allows discarding maneuver days, since the present analysis does not address the issue of maneuver detection. The OD parameters (satellite properties, force models, numerical integrator, arc durations,…) are given in Table *4*.

3.2 Orbit determination uncertainty analysis

3.2.1 Uncertainties considered

The uncertainties in the OD process are considered through a covariance computation. The two main contributors of this covariance in cislunar orbit are the following:

- measurement noise
- uncertainty on the TDOA biases

The uncertainty on the solar radiation parameter does not contribute at first order on the covariance (less than 1 meter in position) and will therefore not be considered in the rest of the study.

[3] RSS: Root Sum Square

	Satellite properties
mass (kg)	1850
surface (m²)	14
Reflection coefficient (-)	1
frequency (GHz)	8.4 (Earth Observation X band)
	Force model
main body	Moon
main body potential	GRAIL350A, 90x90
Solar Radiation Pressure	standard, with Moon eclipses
3rd body	Sun, Earth
	Numerical integrator
name	RKN12(10)
step	Fixed, 10s
arc duration	1 day
estimated parameters	orbital parameters (SRP fixed, ground station biases fixed)
Measurement cadency	3min (considering satellite occultation by the Moon)

Table 4: OD parameters

The uncertainty on the estimated state vector due to a parameter p is computed as follows:

$$Cov(d\vec{X}) = E\left(d\vec{X^t}d\vec{X}\right) = E\left(\left(\frac{\partial \vec{X}}{\partial p}dp\right)^t\left(\frac{\partial \vec{X}}{\partial p}dp\right)\right) = J^t E(dp^t dp)J = J^t Cov(p)J$$

$$J = \frac{\partial \vec{X}}{\partial p}$$

With J the jacobian matrix of the uncertain parameter and estimated state mapping.

3.2.2 Validation of covariance computation

The covariance is validated through the comparison with the results given by Monte-Carlo draws on the uncertain parameters.

Minimum number of Monte-Carlo draws

The minimum number of samples needed for the Monte-Carlo is given using the Wilks approach [3]. This method gives the minimum number of samples so that the probability that a given random variable would be in an interval [I; +∞[is higher or equal to a value β with the confidence level γ.

$$P(P(X \in I) \geq \beta) \geq \gamma \Leftrightarrow n = \frac{\ln(1-\gamma)}{\ln(\beta)}$$

In our case, we want to validate the covariance in position. The random variable is therefore the Mahalanobis distance of this covariance. This distance squared follows a χ^2 law distribution with 3 degree of freedom. By applying a value of 3 on the Mahalanobis distance and a confidence level of 99.999%, we get:

$$\beta = 0.9707, \gamma = 0.99999$$
$$n = 388$$

There need to be at least 388 samples in our Monte-Carlo validation. Adding some margin, we consider 1000 samples.

Monte-Carlo draws methodology

The methodology is the following:

- Generate noise-free measurements from the reference trajectory and attribute an uncertainty to each measurement corresponding to a gaussian distribution (See Table 3 for measurement noise)
- Apply an uncertainty to the TDOA biases (See Table 3)
- Perform an OD on it and compute the covariance out of the OD process
- For each Monte-Carlo draw:
    - Generate a set of noisy measurements by applying a gaussian noise on the noise free measurements (See Table 3)
    - Generate random biases with gaussian distribution (See Table 3)
    - Perform an OD on this new set of measurements
    - Compare to the original OD

If the covariance is carefully computed, the Monte-Carlo should therefore 'reconstruct' the estimated covariance. In order to assess the good reconstruction of the covariance, we use the similarity distance between two covariance matrices described in [4]:

$$sim(Cov_1, Cov_2) = \frac{trace(Cov_1 Cov_2)}{\|Cov_1\|\|Cov_2\|}$$

A similarity of one means that the covariances are similar, and zero that the covariances differ to a maximum extent. Here, the norm corresponds to the Frobenius norm.

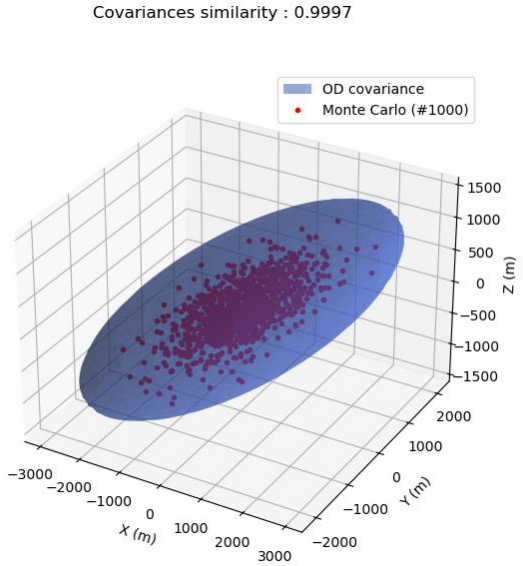

Fig. 8: OD covariance in position and corresponding Monte Carlo draws

Fig. 8 shows the OD covariance ellipsoid and all the Monte Carlo fit results. We notice that all the Monte-Carlo fits lie in the covariance with a similarity index of 0.9997, which validates the covariance computation.

3.3 Impact of the use of very long baselines on cislunar orbit determination

3.3.1 Methodology

During this phase, we compare the two following configurations:

- Short baseline configuration: baselines are limited to each region (CONUS, EMEA, APAC, Oceania Pacific)
- Long (and short) baseline configuration: baselines are built using all the ground stations in visibility, independent of any regional consideration. In this configuration, we end up with both short and long baseline configurations. This allows for maximum coverage. Indeed, when long baselines have no common visibilities, the system switches to the short base configuration.

Fig. 9 provides an example of the short and long baseline configurations while Fig. 10 gives an example of the evolution of the ratio between long and short baseline and also the network baseline mean distance over a measurement arc.

Fig. 9: CONUS-EMEA long and short baseline configurations

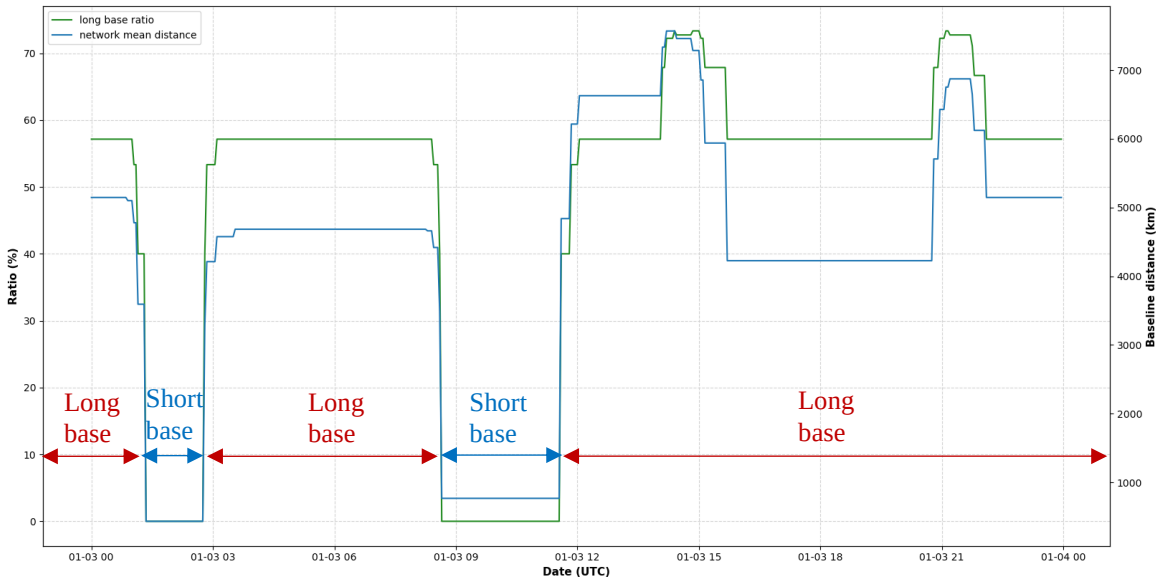

Fig. 10: Long base ratio and network baseline mean distance evolution example

We perform then a set of orbit determinations with parameters described in Table *4* in both configurations from the 20th September 2009 to the 15th February 2010.

3.3.2 Results

A first interesting result lies in the portion of the orbit covered by the measurements (See Fig. 11). This plot is a polar representation of the true latitude argument of the orbit. The orbit is therefore represented by a circle. The measurements are represented by red dots. A full coverage of the orbit by the measurements would result in a full red circle. For low cislunar orbits such as LRO, this coverage is independent on the configuration (short or long baselines). We can see in Fig. 12 that the mean portion of the orbit covered by the measurement is 71%. This provides a very good diversity in the observation of the orbit which is very important in orbit determination.

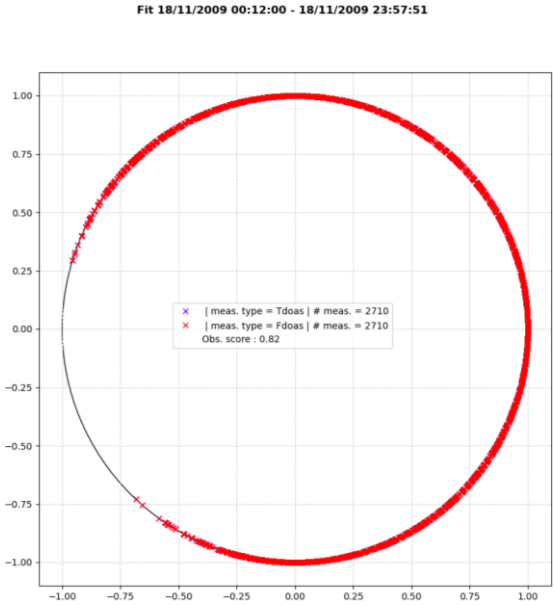

Fig. 11: True latitude argument distribution of the measurements for one fit

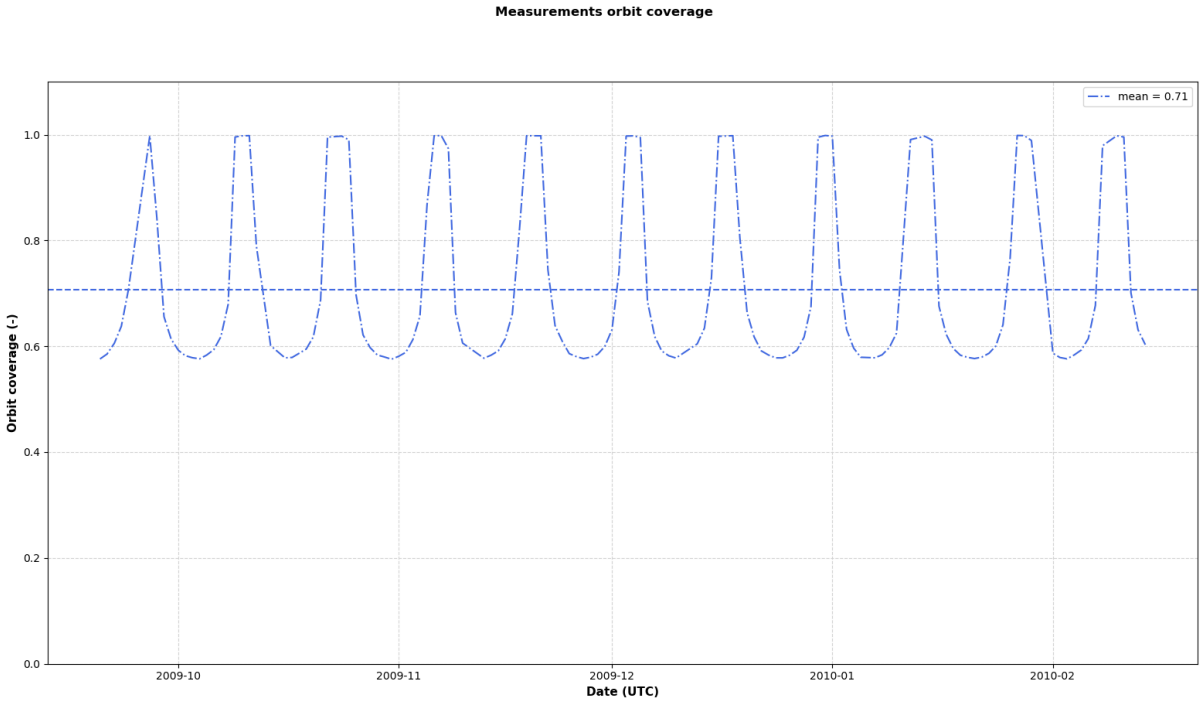

Fig. 12: Mean orbit coverage by the measurements for all fits

Secondly, Table 5 provides the 0.95 quantile Keplerian parameter errors and covariance at date of fit (which corresponds to the date of the first measurement). The third column gives the ratio between short and long baseline configuration, which we can also call the 'gain' in performance due to the long baseline configuration. Except for the semi-major axis error which is equivalent (gain of ~1) in both configurations, all the other gains are very high.
If one wants to pick a particular significant result, one could look at the position error and the associated 97.07% probability distance extracted from the covariance matrix in position (which corresponds to an equivalent Mahalanobis distance of 3 for the 3 degrees of freedom $\chi_2$distribution on the covariance matrix in position). Indeed, in the short baseline configuration, the position error is 3.6km +/- 3.4km (3σ equivalent) instead of 115m +/- 510m for the long baseline configuration confirming the benefit of using the long baseline configuration.

Parameter	**0.95 quantile**		
	Short baseline configuration	**Long baseline configuration**	**Short / Long**
Semi-major axis error (m)	98.7	103.5	0.95
Eccentricity error (-)	4.69E-04	4.94E-05	9.49
Inclination error (mdeg)	76.1	3.1	24.55
RAAN error (mdeg)	52.7	1.7	31.00
True latitude argument error (mdeg)	71.7	4.1	17.49
Position error (m)	3615.6	114.8	24.97
σ Semi-major axis (m)	1729.7	195.4	8.85
σ eccentricity (-)	0.2331	0.02724	8.56
σ Inclination(mdeg)	43.9	4.7	9.34
σ RAAN (mdeg)	37.8	3.9	9.69
σ True latitude argument (mdeg)	29.1	3.2	9.09
0.9707 probability distance (m)	3380.2	507.6	6.66

Table 5: 0.95 quantiles for long and short baseline configuration at date of fit.

Fig. 13 and Fig. 15 provides the cumulative distribution functions respectively of the Keplerian and position error and their associated standard deviation between estimated orbit and reference orbit. We compute also the maximum pointing error over the fit period as seen from the ground stations. The temporal evolution of these errors is given in Fig. 14.
The 0.95 quantile of the maximum pointing error for short and long baseline is respectively 2.38 arcsec and 0.12 arcsec. This value gives an idea of the pointing accuracy achievable with the long baseline configuration. The corresponding gain in accuracy with respect to the short baseline configuration is of 19.1.

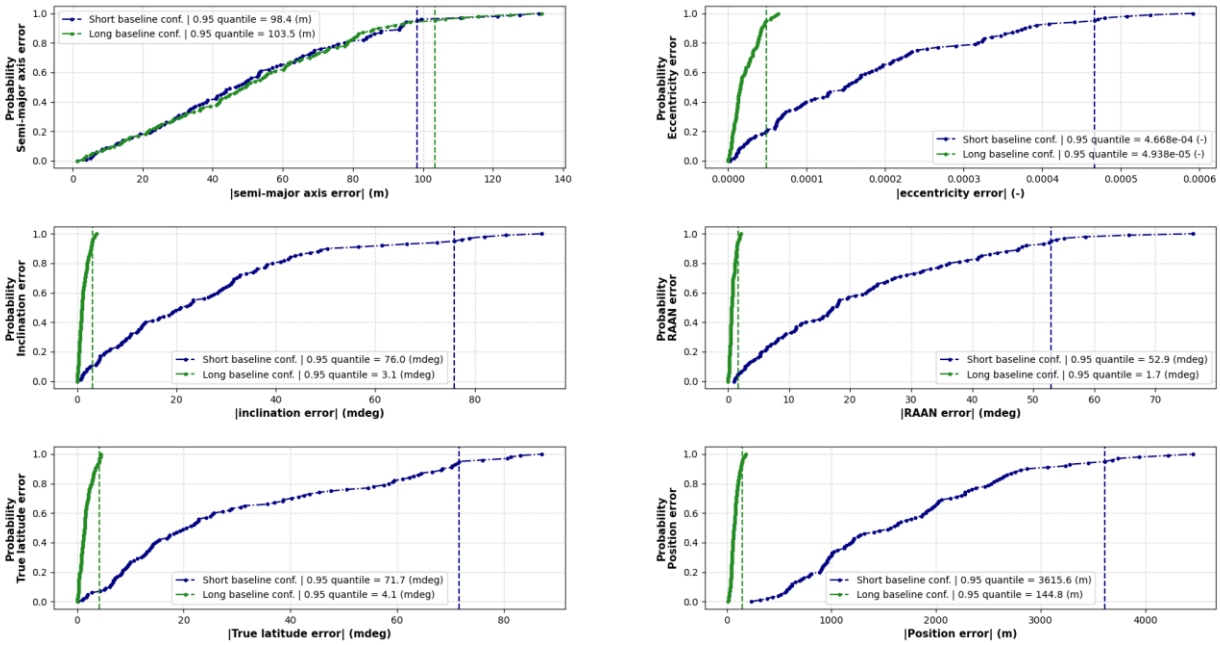

Fig. 13: Keplerian parameters and position error cumulative distribution functions

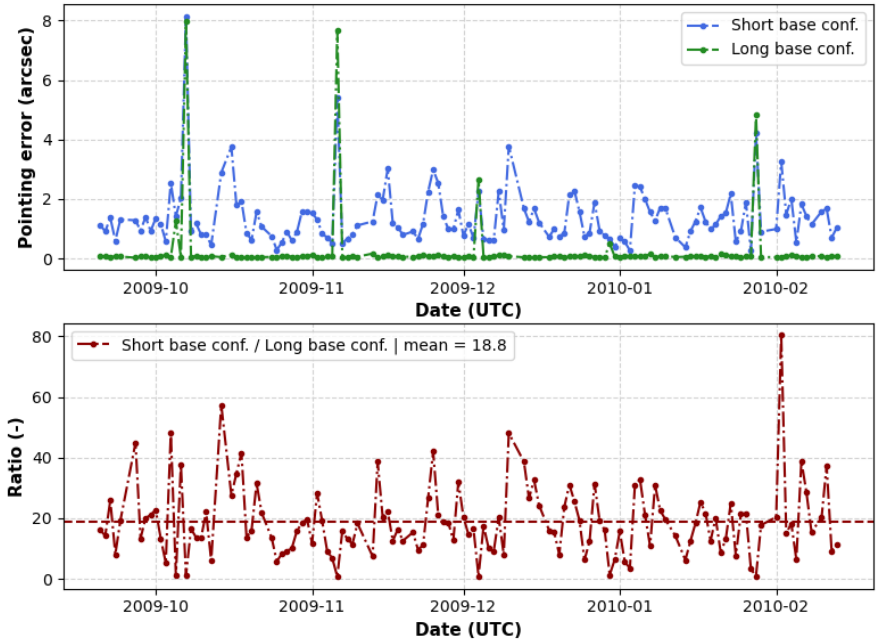

Fig. 14: Maximum pointing error in station for all fits

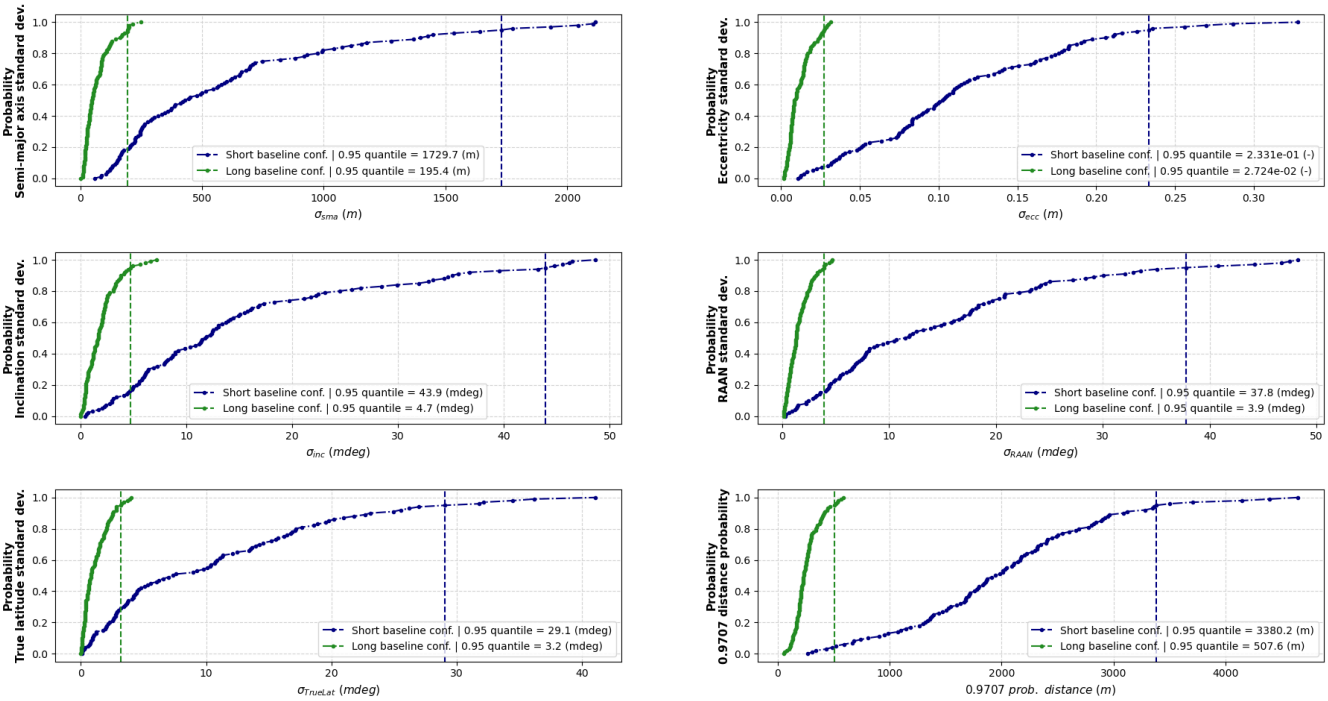

Fig. 15: Keplerian parameters and position standard deviation cumulative distribution functions

3.3.3 Observability analysis

In this section, we want to assess the observability of the estimated parameters for each configuration (long and short baseline). To do so, we propose a method based on the spectral analysis of the least-squares normal matrix. The weighted least squares normal matrix comes directly from the normal equation:

$$\overline{x} = (H^t W H)^{-1} H W \, \overline{y} = N^{-1} H W \overline{y}$$

With:

$\overline{x} = \begin{bmatrix} x_1 \\ \cdots \\ x_n \end{bmatrix}$, the vector of estimated parameters,

$\overline{y} = \begin{bmatrix} \overline{y_1} \\ \cdots \\ \overline{y_l} \end{bmatrix}$ and $\overline{y_l} = \overline{y(t_l)} = \begin{bmatrix} y_1 \\ \cdots \\ y_p \end{bmatrix}$, the p-vector of measurements at time t_i,

H, the jacobian matrix of the measurements with respect to estimated parameters,

N, the normal matrix.

In our case, we express the estimated parameters in terms of circular Keplerian parameters, which are well adapted to low eccentricity LRO orbits (~5.2e-3 over the studied period). We therefore have:

$$\overline{x} = \begin{bmatrix} x_1 \\ \cdots \\ x_6 \end{bmatrix} = \left[a, e_x, e_y, i, \Omega, \alpha\right]^t$$

With:
a: semi-major axis of the orbit
$e_x = e * \cos(\omega)$: first component of the eccentricity vector
$e_y = e * \sin(\omega)$: second component of the eccentricity vector
i: inclination
Ω: Right ascension of the ascending node of the orbit
$\alpha = \omega + \nu$: True latitude argument
ω: argument of perigee
ν: True anomaly

The eigen vectors of the normal matrix gives an information on the direction of observability in the estimated parameter space. For example, a normalized eigen vector of [1, 0, 0, 0, 0, 0] would indicate an observability in the semi-major axis direction while a normalized eigen vector of [0, 0.5, $\frac{\sqrt{3}}{2}$, 0, 0, 0] would indicate an observability in the $\bar{v} = 0.5e_x + \frac{\sqrt{3}}{2}e_y$ direction. The eigen values on their side, would indicate the magnitude of the observability in the considered direction. We therefore define the overall observability on parameter x_i as follows:

$$obs(x_i) = \sum_{j=1}^{6} \lambda_j |\overline{V_j}.\overline{e_i}|$$

With λ_j being the eigen value associated to the normalized eigen vector $\overline{V_j}$ and $\overline{e_i}$ the unit vector in the direction of parameter x_i. In other terms, we add the absolute value of the projection of the eigen vectors in the direction of the component of interest. This gives us the overall observability in the direction of the component.
We perform this computation for each fit in both short and long baseline configurations. For each fit, we also perform a 'reference' fit on position and velocity measurements from the reference trajectory, which would give the maximum achievable observability of the estimated parameters.
We then compare for each fit the overall observability of each parameter with the one obtained for the reference fit. The ratio gives access to an observability level (between 0 and 1) with respect to the fit:

$$obs_{level}(x_i) = \frac{obs(x_i)}{obs_{ref}(x_i)}$$

The results are summarized in Table 6 and the results for each fits and parameters are given in Fig. 16.

Parameter	**Mean observability level**		
	Short baseline	**Long baseline**	**Short / long**
a	1.38E-08	5.43E-06	393.5
e_x	1.39E-06	4.22E-04	303.6
e_y	3.92E-06	1.34E-03	341.8
i	5.86E-08	3.79E-05	646.8
Ω	1.03E-07	2.60E-05	252.4
α	2.73E-08	1.04E-05	381.0

Table 6: Mean observability level for all fits

We see that the long baseline configuration allows for a significant increase in the overall observability, with a mean ratio of 386.

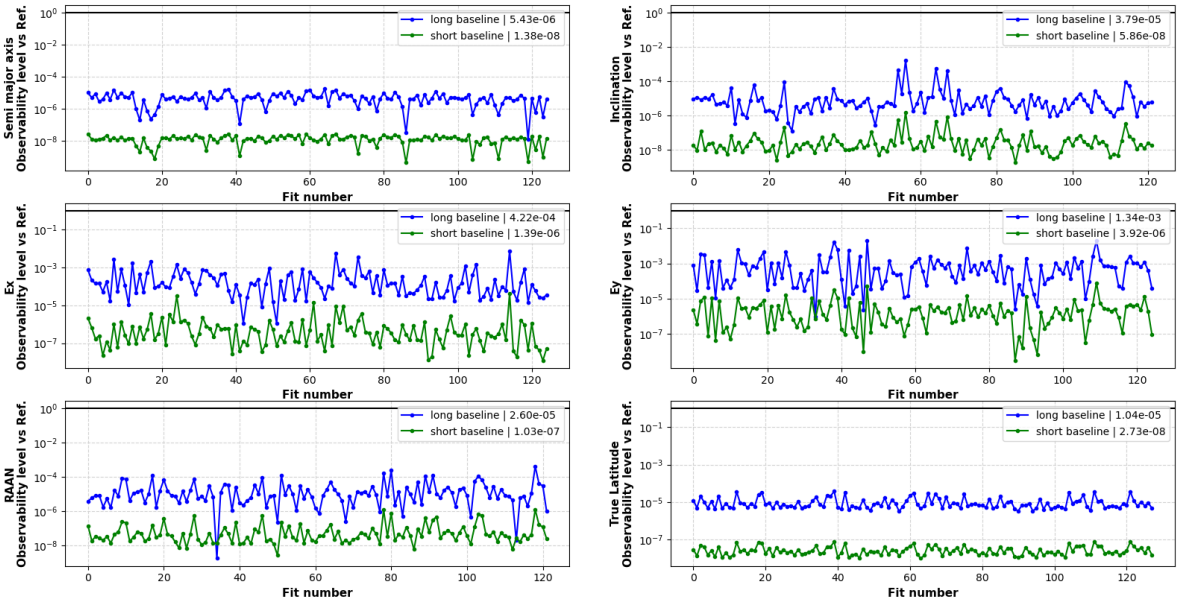

Fig. 16: Observability level on estimated parameters for fit and configuration

3.4 Orion (Artemis I) tracking activities

3.4.1 Tracking

Using its S-band CONUS tracking network (short baseline configuration only), Safran Data Systems was able to successfully track and collect measurement (TDOA & FDOA) on Orion Artemis I mission on its way to the Moon and during a part of its trajectory in Distant Retrograde Orbit (DRO). With the collected measurements, Safran was able to perform two orbit determinations on the outbound trajectory and part of DRO (See Fig. 17)
The reference trajectory is retrieved from JPL Horizons. Table 7 gives the satellite characteristics used for the orbit determinations.

Parameter	Satellite properties
Area over Mass (kg/m²)	0.00442 (estimated from JPL ephemeris)
Reflection coefficient (-)	1
frequency (GHz)	2.2165
	(S band)

Table 7: Satellite characteristics used for Orbit Determination

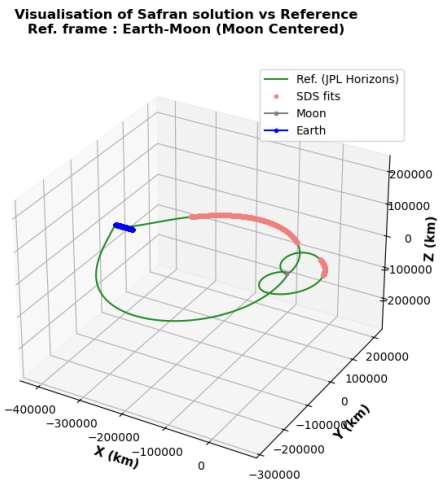

Fig. 17: SDS orbit determination vs reference trajectory in Earth-Moon reference frame.

3.4.2 Fit results

First fit

The first orbit determination covers the period from the November 17, 13h30Z to the November 18, 18h56Z. Table 8 and Table 9 give respectively the orbit propagator and orbit determination configurations for the fit. Please note that the measurement noise is directly a product of the Cross Ambiguity Function (CAF) and is not fixed 'a-priori' at orbit determination initialization.

We can see that the measurement residuals at the end of fit (See Fig. 18 and Fig. 19) are quite good for both TDOA and FDOA with respectively RMS values of 54ns and 0.8Hz. However, the comparison with the reference orbit gives an RMS error of 38.6km equivalent to a mean error as seen from the ground stations of ~3 mdeg (See Fig. 20).

Parameter	**Force model**	
	Fit #1	***Fit #2***
main body	Earth	Moon
main body potential	JGM3 (36x36)	GRAIL350A (8x8)
SRP	standard, with Earth eclipses	standard, with Moon eclipses
3rd body	Sun, Moon	Sun, Earth
	Numerical integrator	
name	RKN12(10)	
step	Fixed, 30s	

Table 8: Orbit propagator configurations

Parameter	**Orbit Determination**	
	Fit #1	***Fit #2***
Measurements	TDOA & FDOA	
Position & velocity	Estimated	
Ground delays	Fixed	
Area over mass	Fixed	
Date of first measurement	17/11/2022 13:29	26/11/2022 17:45
Date of last measurement	18/11/2022 18:56	28/11/2022 01:55
Fit duration (days)	1.23	1.34
Number of measurements	402	380
Measurement noise	From CAF	

Table 9: Orbit determination configurations

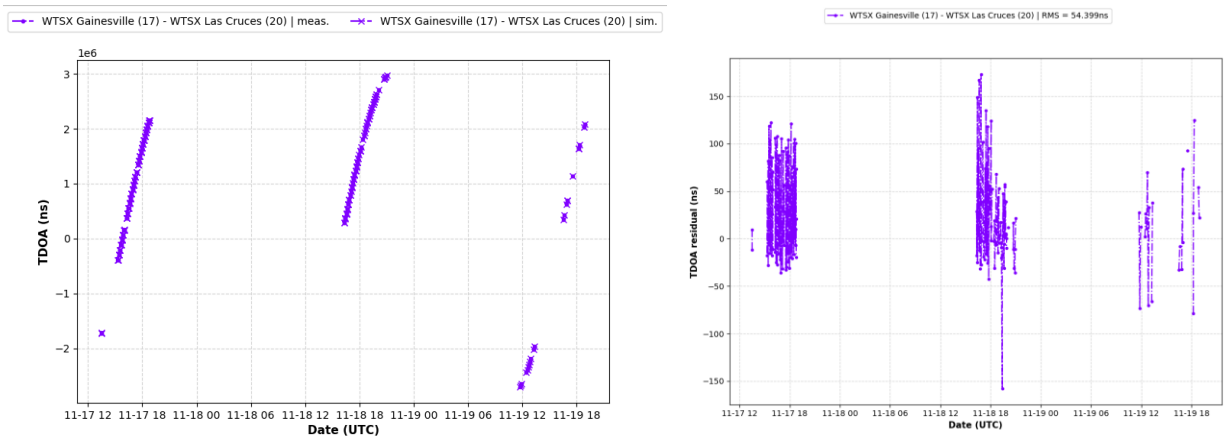

Fig. 18: TDOA measurements Fit #1 (left), TDOA residuals Fit #1 (right)

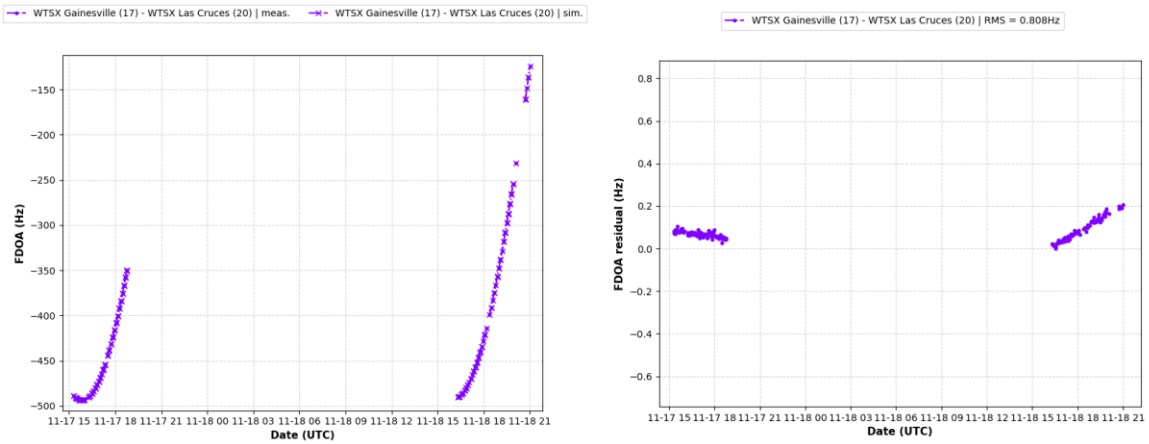

Fig. 19: Fit #1 FDOA measurements (left), FDOA residuals (right)

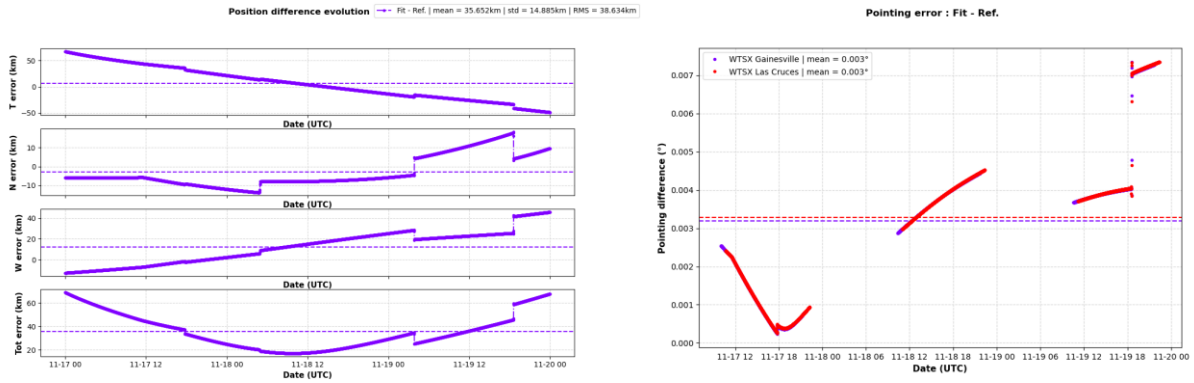

Fig. 20: Fit#1 Position error vs reference in TNW[4] ref. frame (left), pointing error vs. reference from ground stations (right)

[4] TNW local orbital frame
T: unit vector along velocity, W: unit vector normal to the orbital plane, N: such that TNW is a direct basis.

Second fit

The second orbit determination covers the period from November 26, 17h45Z to November 28, 01h55Z. (See Table 8 and Table 9 for orbit propagator and orbit determination configurations).
We can see that the measurement residuals at the end of fit (See Fig. 21 and Fig. 22) are again quite good for both TDOA and FDOA with respectively maximum RMS values of 31ns and 10Hz. Again, the comparison with the reference orbit is not that good and we obtain an RMS error of 127km which represents a mean angular error in station of ~15 mdeg (See Fig. 23).

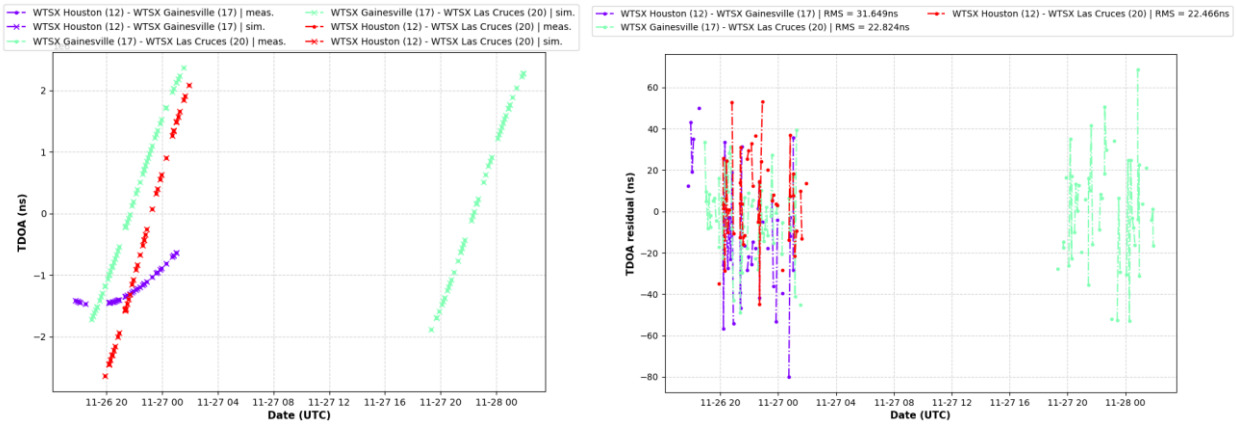

Fig. 21: Fit #2 TDOA measurements (left), TDOA residuals (right)

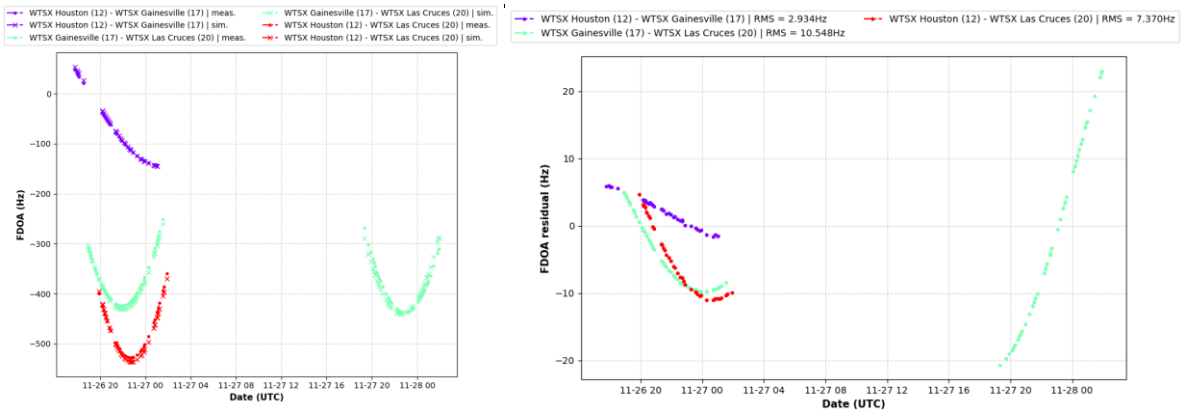

Fig. 22: Fit #2 FDOA measurements (left), FDOA residuals (right)

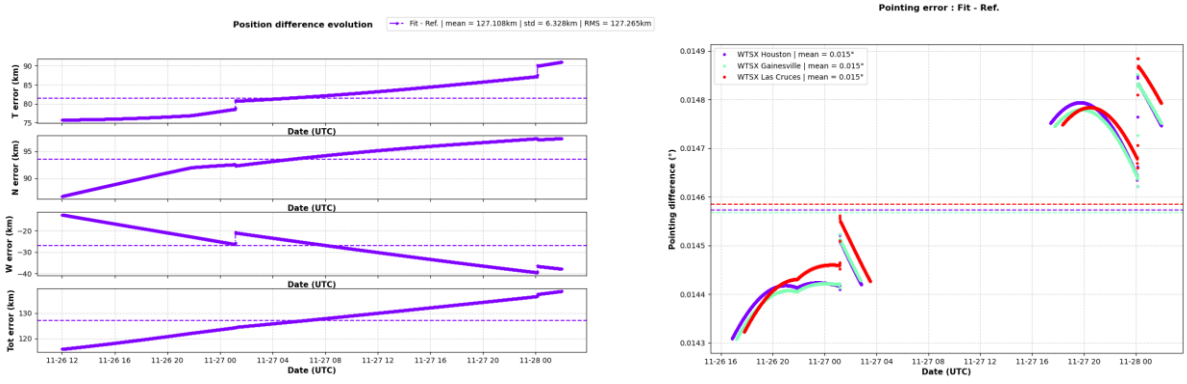

Fig. 23: Fit#2 Position error vs reference in TNW ref. frame (left), pointing error vs. reference from ground stations (right)

3.4.3 Performance analysis

The orbit determination performance does not agree with the short baseline results presented in the LRO analyses. Indeed, with the short baseline configuration, we ended up with a position error of 3.6km and a 97.07 probability distance of 3.4km, which is well below the obtained performance obtained in the two orbit determinations performed on Orion Artemis I.
This drop in performance can be explained by:

- The very high dynamic of Orion spacecraft. Indeed, Orion, performed numerous trajectory corrections maneuvers, which are not present in our model (See Fig. 24, [5]). On this figure, each dot represents a thruster activity along the trajectory represented in Earth-Moon reference frame. These un-modelled maneuvers are likely present in our measurement arc and greatly perturb the orbit determination.
- Contrarily to the previous analyses, the measurements were obtained using only one region (CONUS), instead of including data from all four regions. This directly affects the coverage of the orbit and therefore the accuracy of the orbit fit.

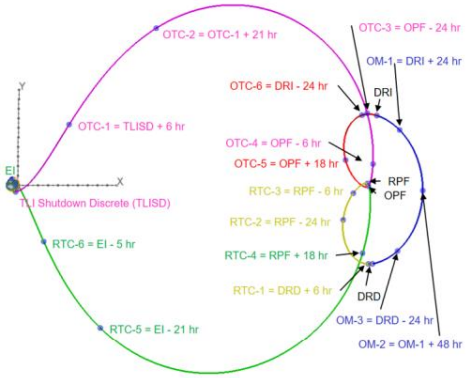

Fig. 24: Orion's spacecraft trajectory maneuvers.

Anyway, these results show Safran Data System's ability to collect measurement on cislunar objects, at very high distances and are very encouraging for future experimentations.

4. CONCLUSION

In this work we presented Safran Data Systems past and present works on cislunar activities. We particularly showed how passive RF can be of interest for tracking cislunar satellites and how the use of a long baseline configuration could greatly enhance the performance of the orbit determination of cislunar objects in trajectories similar to the LRO. Indeed, with Safran Data System's network, we have showed that in the long baseline configuration, we could theoretically achieve an accuracy of 115m in position with an associated 3σ covariance of ~500m. This performance is very encouraging and could be of great interest for accurate cislunar tracking purposes.
We also presented the results obtained on real data during Orion Artemis I tracking which underline Safran Data System's ability to collect measurements on such missions. In this case, the performance was limited due to the very perturbed dynamic of Orion spacecraft by frequent trajectory corrections that occurred along the flight.
A follow-on effort could involve testing the long baseline configuration on real measurements on missions such as Lunar Reconnaissance Orbiter, Danuri, Themis A and B in order to assess the real performance achievable. Another interesting analysis would be to use this long baseline configuration for maneuver detection and characterization purposes. Last but not least, tracking objects beyond cislunar orbits such as orbits around the Lagrange points of the Earth-Moon system or the Sun-Earth system (e.g. JWST, SOHO) is clearly something that will be a major focus in the coming years.

5. REFERENCES

[1] B. A. Archinal et al., Report of the IAU Working Group on Cartographic Coordinates and Rotational Elements: 2009, *Celestial Mechanics and Dynamical Astronomy*, Vol. 109, 101-135, 2009.

[2] Michael Mesarch, Mark Beckman, David Folta, Rivers Lamb, and Karen Richon. Maneuver Operations Results from the Lunar Reconnaissance Orbiter (LRO). SpaceOps 2010 Conference, Huntsville, Alabama, April 25-30, 2010.

[3] S. S. Wilks, Determination of Sample Sizes for Setting Tolerance Limits, *The Annals of Mathematical Statistics*, Vol.12, pp. 91-96, 1941.

[4] Markus Herdin, Nicolai Czink, Hüseyin Ozcelik, Ernst Bonek. Correlation Matrix Distance, a Meaningful Measure for Evaluation of Non-Stationary MIMO Channels. Proceedings of VTC 2005 Spring Stockholm, Stockholm, September 28, 2005.

[5] Randy A. Eckman, Charles Barrett, Amelia L. Batcha, and Brian J. Killeen. Trajectory operations of the Artemis I mission. AAS/AIAA 2023Conference, Big Sky, Montana, August 13-17, 2023.

[6] Byron D. Tapley, Bob E. Schutz, George H. Born. *Statistical Orbit Determination*, Elsevier Academic Press, 2004.